

Computations of flow over a flexible plate using the hybrid Cartesian/immersed boundary method

Sangmook Shin^{*,†}, Sung Yong Bae, In Chul Kim, Yong Jig Kim and Ja Sam Goo

*Department of Naval Architecture and Marine Systems Engineering, Pukyong National University,
Daeyeon, Busan 608-737, Korea*

SUMMARY

A hybrid Cartesian/immersed boundary code is developed and applied to interactions between a flexible plate and a surrounding fluid. The velocities at the immersed boundary (IB) nodes are reconstructed by interpolations along local normal lines to an interface. A new criterion is suggested to distribute the IB nodes near an interface. The suggested criterion guarantees a closed fluid domain by a set of the IB nodes and it is applicable to a zero-thickness body. To eliminate the pressure interpolation at the IB nodes, the hybrid staggered/non-staggered grid method is adapted. The developed code is validated by comparisons with other experimental and computational results of flow around an in-line oscillating cylinder. Good agreements are achieved for velocity profiles and vorticity and pressure contours. As applications to the fluid–structure interaction, oscillations of flexible plate in a resting fluid and flow over a flexible plate are simulated. The elastic deformations of the flexible plate are modelled based on the equations of motion for plates considering the fluid pressure as the external load on the plate. Two non-dimensional parameters are identified and their effects on the damping of the plate motion are examined. Grid convergence tests are carried out for both cases. Copyright © 2007 John Wiley & Sons, Ltd.

Received 19 July 2006; Revised 18 January 2007; Accepted 18 January 2007

KEY WORDS: fluid–structure interaction; immersed boundary node; hybrid staggered/non-staggered grid; zero-thickness body; elastic deformation

1. INTRODUCTION

The interactions between flexible structures and the surrounding fluid are common in various areas, such as the flow in the human cardiovascular system and a liquid sloshing in a tank. Recently a variety of methods are proposed to treat the deformations of the fluid domain as the interfaces move. Those methods can be categorized into two classes: boundary conforming methods and

^{*}Correspondence to: Sangmook Shin, Department of Naval Architecture and Marine Systems Engineering, Pukyong National University, Daeyeon, Busan 608-737, Korea.

[†]E-mail: smshin@pknu.ac.kr

Contract/grant sponsor: Underwater Vehicle Research Center

non-boundary conforming methods. For the boundary conforming methods, many methods are suggested based on the arbitrary Lagrangian–Eulerian (ALE) formulation [1–6]. Since the mesh conforms to the body boundary at all times in the ALE methods, the rapid changes of dependent variables in the boundary layer can be resolved effectively. However, it is not easy to maintain the quality of the deformed grid especially for the cases where the boundaries undergo large deformations.

The non-boundary conforming methods can handle more general deformations of the fluid domain because the background grid is independent of the interface configurations. The immersed boundary method proposed by Peskin [7] has been widely used for the fluid–structure interaction problems [8–11]. The main difficulty of the immersed boundary method is related to the spreading of the forcing function over a few nodes, which increases the resolution requirements near the interface. Several methods are suggested to prevent the smearing near the interface. In the immersed interface method [12–14], the jump condition is introduced to maintain the sharpness of the interface. The cut-cell or Cartesian method can track a sharp interface by modifying the grid cells near the interface [15–17]. However, the generation of irregularly shaped cells, which can degrade the accuracy and robustness of the scheme, may not be avoidable for complicated interfaces.

Gilmanov and Sotiropoulos [18, 19] recently introduced the hybrid Cartesian/immersed boundary (HCIB) method. In this method, the IB nodes are distributed inside of a fluid domain near an interface. Then solutions are reconstructed at the IB nodes by the interpolations along local normal lines to the interface. To eliminate the pressure interpolations at the IB nodes, the hybrid staggered/non-staggered grid method is suggested. They modified the original criterion for the IB node distribution based on the distance between a node and an interface in order to handle a zero-thickness body [19]. However, there is ambiguity in the distance criterion to guarantee a closed fluid domain by the set of IB nodes for the case where the grid spacing is varied along an interface. They applied the HCIB method to simulate the fish-like swimming and the flow around a planktonic copepod. Even though the body boundaries undergo very complicated deformations, the motions of the interfaces are prescribed.

In this paper, the HCIB method is expanded to the interactions between a flexible structure and the surrounding fluid, where the motions of the structure should be decided based on the fluid load. We think this is the first application of the HCIB method to the fluid–structure interaction problems where the deformations of an elastic body should be decided based on the fluid load. We suggest a new criterion to distribute the IB nodes, which guarantees a closed fluid domain by a set of IB nodes regardless of grid spacing variations. In addition the suggested criterion is applicable to a zero-thickness body without any difficulties. In Section 2, the details of the numerical scheme are presented. In Section 3, the developed code is validated through comparisons with other experimental and recent computational results on the flow field around an in-line oscillating cylinder. Then the code is applied to simulate the oscillations of a flexible plate in a resting fluid and the flow over a flexible plate. Finally, some concluding remarks are provided in Section 4.

2. NUMERICAL METHODS

2.1. Governing equations and boundary conditions

The governing equations are the two-dimensional unsteady incompressible Navier–Stokes equations in the Cartesian coordinates, $\{x_i\}$. The governing equations are non-dimensionalized by a fluid

density ρ , a characteristic velocity U and a characteristic length L

$$\frac{\partial u_j}{\partial x_j} = 0 \quad (1)$$

$$\frac{\partial u_i}{\partial t} + u_j \frac{\partial u_i}{\partial x_j} = -\frac{\partial p}{\partial x_i} + \frac{1}{Re} \frac{\partial^2 u_i}{\partial x_j \partial x_j} \quad (2)$$

where u_i are Cartesian velocity components, p is a pressure and Re is a Reynolds number.

The deforming interface of the fluid/solid is discretized by a set of material points on the interface. For those material points, the Lagrangian position vectors and the velocity vectors are given. The boundary of the fluid domain is defined by a set of line segments connecting two neighbouring material points. The velocity distributions on the line segments are interpolated from the velocity vectors at the material points. The boundary conditions for the Eulerian fluid velocity are described by the no-slip condition at the interface at every instant. The hybrid staggered/non-staggered grid approach [19] is used, where the pressure at the boundary node is not required explicitly as explained later.

2.2. Velocity reconstruction at immersed boundary nodes

In the HCIB method, the governing equations are discretized on a Cartesian background grid and the boundary conditions are described at the IB nodes near the fluid/solid interface. At the IB nodes, the velocity vectors are estimated based on the reconstruction of the solution along the local normal line to the interface. To guarantee that the flow solver uses only well-defined dependent variables, a closed fluid domain should be defined by the set of the IB nodes. Gilmanov *et al.* initially suggested a criterion to distribute the IB nodes so that each node included in a fluid domain is classified as an IB node if the node is connected to a node inside of a solid [18]. This criterion guarantees a closed fluid domain by the set of IB nodes. However, this criterion has difficulty in handling a thin body. Gilmanov *et al.* modified the original criterion to distribute the IB nodes, which is based on the distance between a node inside of the fluid domain and the fluid/solid interface [19]. Although the modified criterion can handle a zero-thickness body, there is ambiguity in the appropriate distance to guarantee a closed fluid domain for a grid of non-uniform spacing.

In this study, a new criterion is suggested to distribute the IB nodes. First, a node is classified as a solid node if the node is located inside of a solid. Then a node is classified as an IB node if the node is not a solid node and the node is connected to an edge that crosses the fluid/structure interface. If a node is not an IB node and it is located inside of the fluid domain, the node is classified as a fluid node [20]. Figure 1 shows an example of a fluid/structure interface and IB nodes which are identified based on the present criterion. The present criterion and the original criterion suggested by Gilmanov *et al.* [18] result in the similar distributions of the IB nodes near the interface where the thickness of the body is greater than the grid spacing. However, the additional IB nodes are identified near a sharp edge of the body based on the present criterion. The present criterion can handle a zero-thickness body because the crossing edges can be identified near the interface regardless of thickness of the body. In addition, the present criterion guarantees that there is no edge connecting a fluid node to a solid node. This fact is important because it ensures that the flow solver does not require an undefined dependent variable for the hybrid staggered/non-staggered grid method as explained later. The identification of the IB nodes based on the present

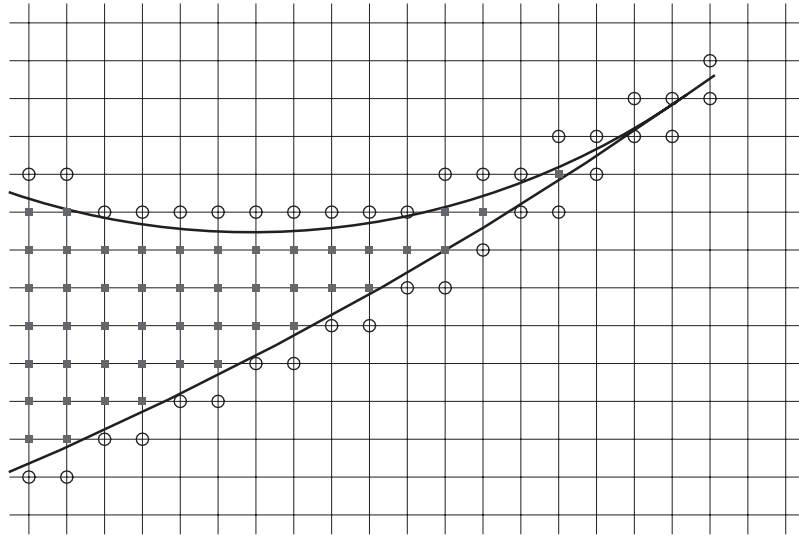


Figure 1. A background Cartesian grid, a fluid/solid interface (line), solid nodes (filled rectangles) and IB nodes (open circles) identified based on the present criterion.

criterion and the search for the neighbouring fluid nodes for the velocity reconstruction can be carried out more efficiently by using a preliminary checking algorithm which decides the overlap between a rectangle containing the given inside node and segments on the boundary. However, for two-dimensional cases, the identification of the IB nodes and the search for the neighbouring fluid nodes do not increase the total calculation time significantly even though the preliminary checking algorithm is not adapted.

The key idea of the HCIB method is the description of the velocity boundary conditions at the IB nodes based on the interpolations along the local normal lines to the body surface [18, 19]. Figure 2 shows the reconstruction of the velocity at an IB node based on the interpolation along the local normal line to the body surface. For each IB node, a line is selected which passes through the IB node and intersects the body surface, S in Figure 2, at right angle. If the body surface contains sharp corners, such lines may not be defined for some IB nodes near the sharp corners. For those IB nodes, lines connecting the IB nodes and the closest points on the body surface replace the local normal lines. Once the interpolation line for each IB node is selected, the line is extended from the IB node to an edge of the background Cartesian grid, E in Figure 2. The velocity vector at the point where the interpolation line crosses the body surface S is already given as the velocity boundary condition at every instant. At the other end point of the interpolation line, where the interpolation line crosses the internal edge of the Cartesian grid E , the velocity vector is estimated based on the two intermediate velocity vectors at both end nodes of the edge, $N1$ and $N2$ in Figure 2, during the iteration procedure of the flow solver. In this study a linear interpolation is used to estimate the velocity vector at the point on the internal edge E

$$\phi_E^l = \frac{1}{d_{N1,E} + d_{N2,E}} (d_{N2,E} \phi_{N1}^l + d_{N1,E} \phi_{N2}^l) \quad (3)$$

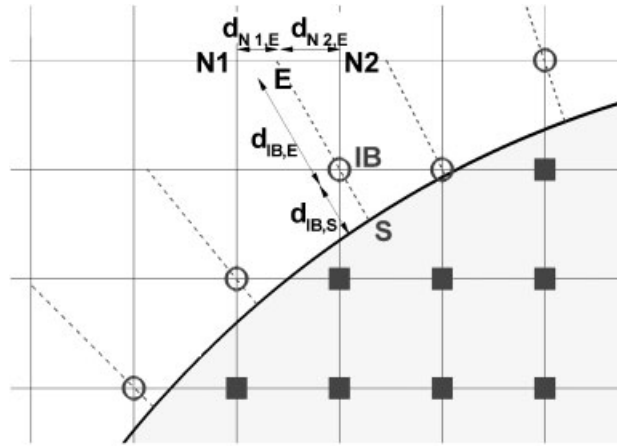


Figure 2. Velocity reconstruction at an IB node by the interpolation along the local normal line to the interface. IB: IB node; S : point on the interface; E : point on an internal edge; $N1$, $N2$: two end nodes of the internal edge.

where ϕ_E^l is a velocity component at the crossing point on the internal edge, ϕ_{N1}^l and ϕ_{N2}^l are velocity components at the two end nodes of the internal edge at l th iteration step of the flow solver and $d_{N1,E}$ and $d_{N2,E}$ are two distances from the crossing point E to the two end nodes $N1$ and $N2$. Finally, the velocity vector at an IB node is estimated based on the distances from the IB node to the end points of the interpolation line $d_{IB,E}$ and $d_{IB,S}$. In this study a linear variation of a velocity along the local normal line is assumed

$$\phi_{IB}^l = \frac{1}{d_{IB,E} + d_{IB,S}} (d_{IB,E} \phi_S + d_{IB,S} \phi_E^l) \quad (4)$$

where ϕ_{IB}^l is the estimated velocity component at the IB node at l th iteration step and ϕ_S is the velocity component at the crossing point on the body surface S .

2.3. Flow solver using the hybrid staggered/non-staggered grid

For the velocity reconstruction at the IB nodes, the use of the non-staggered grid is natural. However, a flow solver based on the non-staggered grid may cause difficulties for the HCIB method. In the HCIB method, the dependent variables should be reconstructed near the body boundary using the interpolation along the local normal line. Compared with the interpolation of velocity near a body boundary, the interpolation of pressure near the body boundary may not be accurate because of the following two facts. Although the Dirichlet-type boundary conditions are given for the velocity, only an approximation for the normal derivative of the pressure is available on the body boundary. In addition, the pressure field near the body may change abruptly due to the deformation of the fluid/structure interface in the incompressible flow. For the staggered grid, the pressure boundary condition is not required explicitly near the body boundary so that only the velocity vectors need to be reconstructed at the IB nodes. Contrary to the conventional immersed boundary method, the present method which is based on the HCIB method using the hybrid staggered/non-staggered grid method does not require any additional treatment to get a

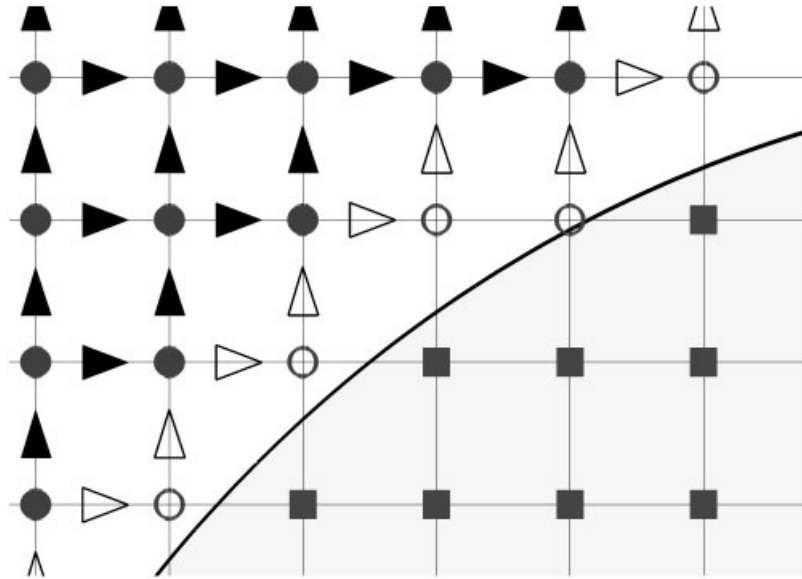


Figure 3. The hybrid staggered/non-staggered grid method. Open circles: non-staggered u and v reconstruction. Open triangles: velocity boundary conditions for the staggered grid. Filled circles: residuals of convection and diffusion terms, calculated pressure, interpolated non-staggered velocities. Filled triangles: interpolated residuals of convection and diffusion terms, calculated staggered velocities.

smooth pressure distribution near moving boundaries. Since the pressure is not defined at the IB nodes in the present method, an extrapolation is necessary to estimate the pressure distribution on the boundary. However, the pressure calculation procedure is identical with the conventional staggered grid approach once the velocities are reconstructed at the IB nodes regardless of the movement of the boundary. Even though additional interpolations are necessary between dependent variables of a staggered grid and a non-staggered grid, the hybrid staggered/non-staggered grid method can provide more advantages by eliminating the pressure reconstruction at the IB nodes.

Figure 3 shows the arrangement of dependent variables for the hybrid staggered/non-staggered grid method near a boundary. All dependent variables of the non-staggered grid are stored at the nodes of the background Cartesian grid. At a mid-point of each edge, the velocity component in the direction of the edge is stored for the staggered grid. The convective and viscous terms of x - and y -momentum equations are calculated at all the fluid nodes using velocities of the non-staggered grid. The second-order, upwind biased scheme is used to discretize the convective term. For a fluid node near an IB node, the second-order upwind biased scheme may require a velocity at a solid node according to the sign of the local convective velocity. In such cases, the first order upwind scheme is used to reduce the stencil. Gilmanov *et al.* showed that such approximation near the body boundary does not affect the second-order accuracy of the scheme based on the log–log variation of the error as a function of the grid spacing [18]. To explain this behaviour, they pointed out that the truncation error of the first-order upwind scheme is related to the second-order spatial derivatives and the second-order spatial derivatives are zero for the linearly varying velocity field near the body boundary. For the viscous term, the central difference is used. Since the velocity

vectors are reconstructed at the IB nodes and a fluid node is guaranteed to be connected to other fluid node or a IB node, as explained in the previous section, the convective and viscous terms of x - and y -momentum equations can be calculated at all the fluid nodes.

For the staggered velocity component near the boundary that is stored at a mid-point of an edge connecting a fluid node and an IB node, an interpolation is used to get a boundary condition for the velocity component of the staggered grid. Based on the reconstructed velocity at the IB node and the intermediate velocity at the fluid node, a linear interpolation is used to get the boundary condition for the staggered grid

$$u_{IB+1/2,j}^l = \frac{1}{2}(u_{IB,j}^l + u_{IB+1,j}^l), \quad v_{i,IB+1/2}^l = \frac{1}{2}(v_{i,IB}^l + v_{i,IB+1}^l) \quad (5)$$

where the nodes of (IB, j) and (i, IB) are IB nodes, the nodes of $(IB + 1, j)$ and $(i, IB + 1)$ are neighbouring fluid nodes and the superscript l indicates l th iteration step of the flow solver. All staggered velocity components that are stored at midpoints of edges connecting two fluid nodes are calculated based on the momentum equations. To calculate the staggered velocity components, the residuals due to the convective and viscous terms are interpolated at the mid-points of the edges connecting two fluid nodes

$$XCD_{i+1/2,j}^l = \frac{1}{2}(XCD_{i,j}^l + XCD_{i+1,j}^l), \quad YCD_{i,j+1/2}^l = \frac{1}{2}(YCD_{i,j}^l + YCD_{i,j+1}^l) \quad (6)$$

where XCD and YCD are the sums of the convective and viscous terms of x - and y -momentum equations, respectively. The pressures at both fluid nodes of an interior edge are used to calculate the pressure gradient for the staggered grid velocity component

$$\left. \frac{\partial p}{\partial x} \right|_{i+1/2,j}^l \approx \frac{p_{i+1,j}^l - p_{i,j}^l}{\Delta x}, \quad \left. \frac{\partial p}{\partial y} \right|_{i,j+1/2}^l \approx \frac{p_{i,j+1}^l - p_{i,j}^l}{\Delta y} \quad (7)$$

The dual time-stepping is used for the time marching and the artificial compressibility is introduced with respect to the pseudo-time [21, 22]. For the physical time, the three-point second-order backward difference formula is used

$$\frac{p_{i,j}^{n+1,l+1} - p_{i,j}^{n+1,l}}{\Delta \tau} + \beta \left(\frac{u_{i+1/2,j}^{n+1,l} - u_{i-1/2,j}^{n+1,l}}{\Delta x} + \frac{v_{i,j+1/2}^{n+1,l} - v_{i,j-1/2}^{n+1,l}}{\Delta y} \right) = 0 \quad (8)$$

$$\begin{aligned} \frac{u_{i+1/2,j}^{n+1,l+1} - u_{i+1/2,j}^{n+1,l}}{\Delta \tau} + \frac{3u_{i+1/2,j}^{n+1,l+1} - 4u_{i+1/2,j}^{n+1,l} + u_{i+1/2,j}^{n+1,l-1}}{2\Delta t} + XCD_{i+1/2,j}^{n+1,l} + \frac{p_{i+1,j}^{n+1,l} - p_{i,j}^{n+1,l}}{\Delta x} &= 0 \\ \frac{v_{i,j+1/2}^{n+1,l+1} - v_{i,j+1/2}^{n+1,l}}{\Delta \tau} + \frac{3v_{i,j+1/2}^{n+1,l+1} - 4v_{i,j+1/2}^{n+1,l} + v_{i,j+1/2}^{n+1,l-1}}{2\Delta t} + YCD_{i,j+1/2}^{n+1,l} + \frac{p_{i,j+1}^{n+1,l} - p_{i,j}^{n+1,l}}{\Delta y} &= 0 \end{aligned} \quad (9)$$

where β is the artificial compressibility parameter and $\Delta \tau$ is the pseudo-time step size. The superscript $(n + 1, l)$ indicates l th pseudo-time step iteration of the $n + 1$ th physical time step. As the iteration with respect to the pseudo-time converges, the dependent variables of $(n + 1, l + 1)$ and $(n + 1, l)$ converge to the dependent variables of $(n + 1)$.

For each physical time step, the new position vectors of the Lagrangian control points are decided and the classifications of the nodes are updated. To avoid the use of undefined dependent variables, there should be no node that is changed from a solid node to a fluid node in one physical time step. It implies that the physical time step Δt should be small so that the interface

never sweeps a whole cell within one physical time step [19]. Although the three-point backward difference formula and the hybrid staggered/non-staggered grid method are used, both schemes do not have effects on the time stepping size because the time stepping size should be kept small to avoid the undefined variables near the moving boundary.

3. RESULTS AND DISCUSSIONS

To validate the developed code, the flow around an in-line oscillating cylinder is computed. The present results are compared with other experimental measurements [23] and recent computations [20] for the velocity profiles and vorticity and pressure fields at several phases of the oscillation. As a test case for the fluid–structure interaction, the oscillations of a flexible plate in a fluid at rest are simulated. Initially, the deformation of the plate is given as its first eigenmode deformation then the plate is released to oscillate in the fluid. The motion of the plate is modelled based on the classical thin-plate mechanics [24, 25]. Finally, the code is applied to simulate the motion of a flexible plate in the cross flow.

3.1. Forced in-line oscillation of a circular cylinder in a fluid at rest

Dütsch *et al.* [23] measured the velocity profiles around a circular cylinder which oscillates in a fluid at rest and Yang and Balaras [20] computed the flow field recently using the embedded-boundary formulation. The forced in-line oscillation of the circular cylinder is described by a sinusoidal motion $x(t) = -A \cos(2\pi ft)$, where A is the amplitude of the oscillation and f is the frequency of the oscillation. There are two non-dimensional parameters in this flow, the Reynolds number $Re = U_{\max} D/\nu$ and the Keulegan–Carpenter number $KC = U_{\max}/fD$, where $U_{\max} = 2\pi fA$ is the maximum velocity of the cylinder, D is the diameter of the cylinder and ν is the kinematic viscosity of fluid. The computation is carried out for the case where the Reynolds and Keulegan–Carpenter numbers are set to $Re = 100$ and $KC = 5$, respectively. The computation starts from the rest. It is confirmed that the flow fields are virtually identical for the same phase of the oscillation after a few strokes. At all the far-field boundary nodes, the dependent variables are extrapolated from the fluid domain. Near the origin, $-3D \leq x \leq 3D$ and $-2D \leq y \leq 2D$, the grid spacing is fixed as $0.02D$ and it is stretched by a factor of 1.05. The size of the computational domain is $50D \times 30D$. The non-dimensional physical time step size is set to $\Delta t = 0.01$. For these parameters, 500 time steps are included in one oscillation.

Figure 4 shows the computed pressure and vorticity contours at three different phase-angles of the oscillation, $\theta = 90, 198$ and 240° . At $\theta = 90^\circ$, a pair of vortices are developing behind the cylinder moving to the right, then the vortices are separated and pushed away by the cylinder moving backward, as observed in the experiments [23]. At $\theta = 198^\circ$, the pressure and vorticity contours are also reported by Yang and Balaras [20]. The agreements between two computational results are very good including the wiggles in the pressure contours in front of the cylinder.

In Figure 5, the computed velocity profiles at $\theta = 90$ and 240° are compared with the measurements [23] and the computations [20] at $x/D = -0.6, 0, 0.6$ and 1.2 . Although Yang and Balaras reported that the agreement between the experimental results (open symbols) and their computational results (lines) is very good, the agreement between the present results (filled symbols) and the computations of Yang and Balaras [20] is much better. The noticeable discrepancy between both calculations can be seen in the u -velocity at $x/D = -0.6$ and $\theta = 90^\circ$. However, at

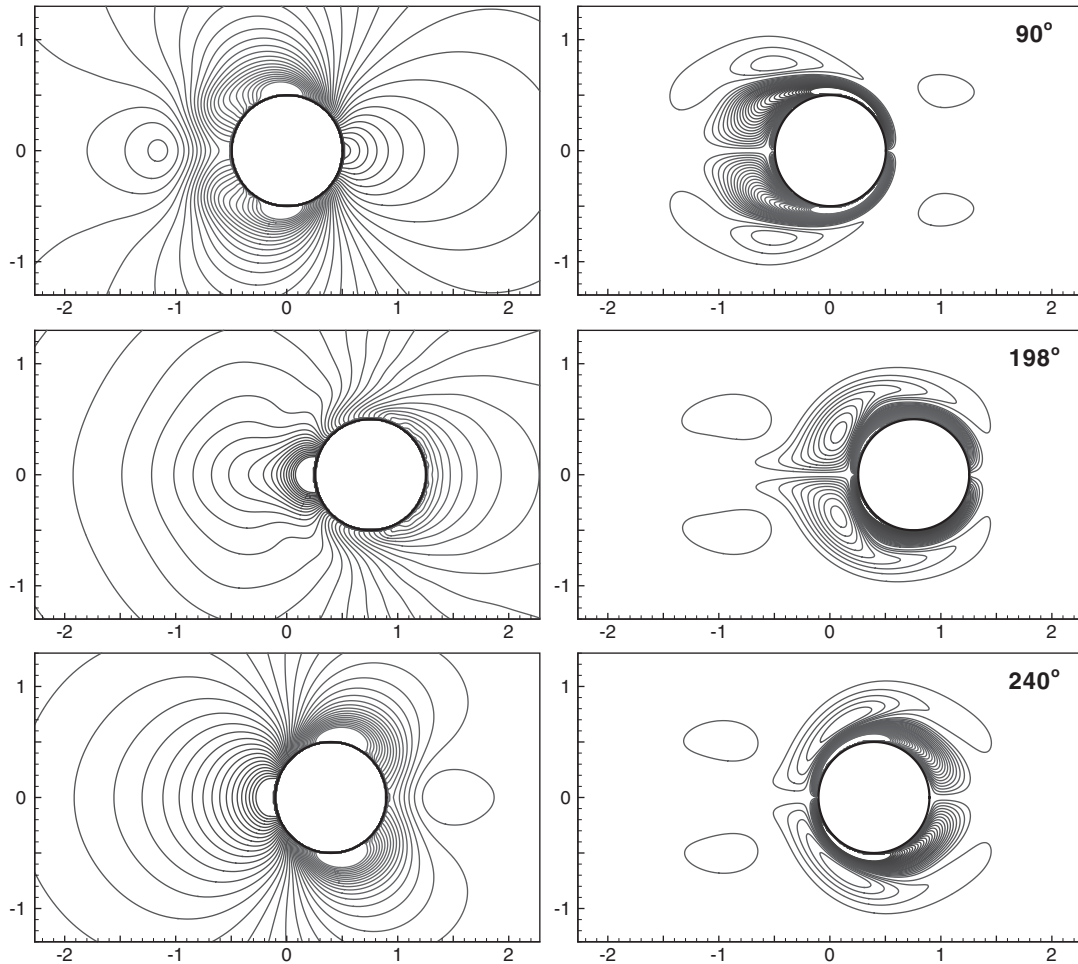


Figure 4. Pressure and vorticity contours around a circular cylinder under forced in-line oscillation in a fluid at rest. $Re = 100$ and $KC = 5$; phase angle $\theta = 90, 198$ and 240° ; $0 \leq P \leq 2$ with intervals of 0.05 and $-7.5 \leq \omega_z \leq 7.5$ with intervals of 0.25.

that location the discrepancies between the measurement and the calculations are more significant. Based on the vorticity contours near the cylinder at $\theta = 90^\circ$ in Figure 4, it is considered that the u -velocity profiles at $x/D = -0.6$ and $\theta = 90^\circ$ can be affected by the vortices which are generated during the previous stroke and pushed away by the cylinder. In Figure 6, contours of the u - and v -velocities at $\theta = 90^\circ$ are shown. It shows that the rapid variations in the velocity near the cylinder are resolved smoothly.

3.2. Oscillations of a flexible plate in a fluid at rest

As an application of the developed HCIB code to the fluid–structure interaction, oscillations of a flexible plate in a fluid at rest are considered. In this study, the motion of the plate is modelled

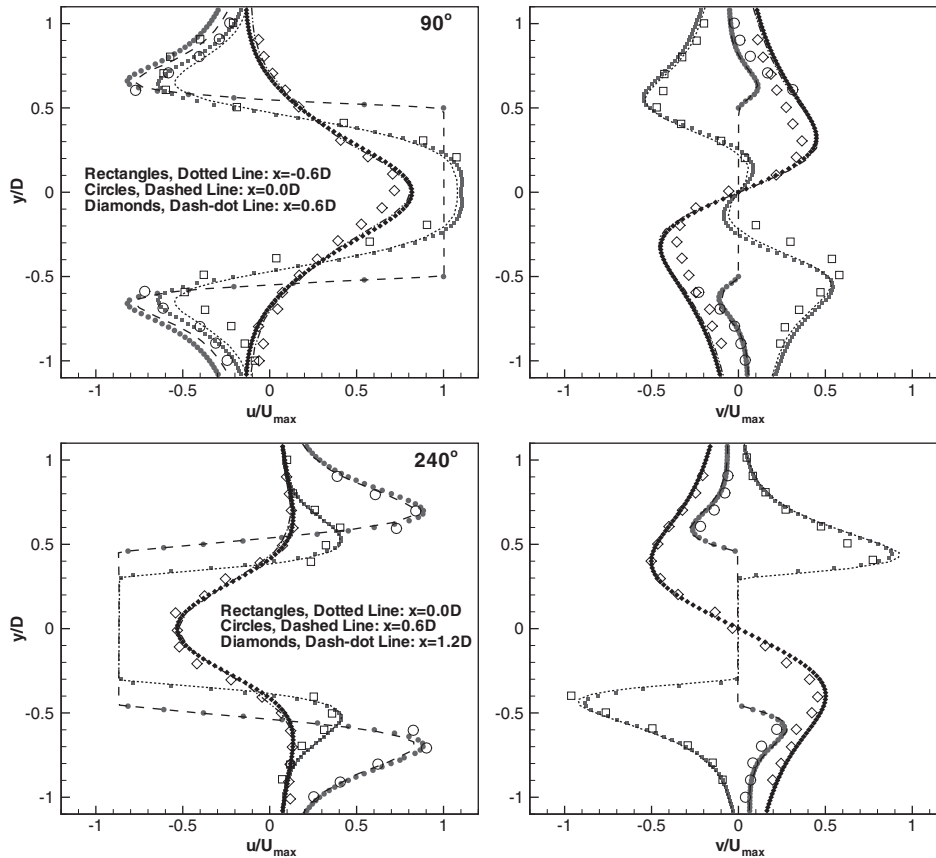


Figure 5. Measured and computed velocity profiles around a circular cylinder under forced in-line oscillation in a fluid at rest. Filled symbols: present computations; lines: computations from [20]; open symbols: measurements from [23]. $Re = 100$ and $KC = 5$; phase angle $\theta = 90$ and 240° .

based on the classical thin-plate mechanics [24, 25]

$$\rho_s h \frac{\partial^2 W}{\partial T^2} + d \frac{\partial W}{\partial T} + B \frac{\partial^4 W}{\partial Y^4} = -\Delta P \quad (10)$$

where $W(Y, T)$, ρ_s , h , d and B are, respectively, deformation, density, thickness, structural damping and flexural rigidity of the plate. In this study, the material damping of the plate is ignored so that $d = 0$. Equation (10) can be non-dimensionalized based on the length of the plate L , the density of fluid ρ_f and the characteristic velocity U

$$\frac{\partial^2 w}{\partial t^2} + C_1 \frac{\partial^4 w}{\partial y^4} = -C_2 \Delta p \quad (11)$$

$$C_1 = \frac{B}{\rho_s U^2 h L^2}, \quad C_2 = \frac{\rho_f L}{\rho_s h} \quad (12)$$

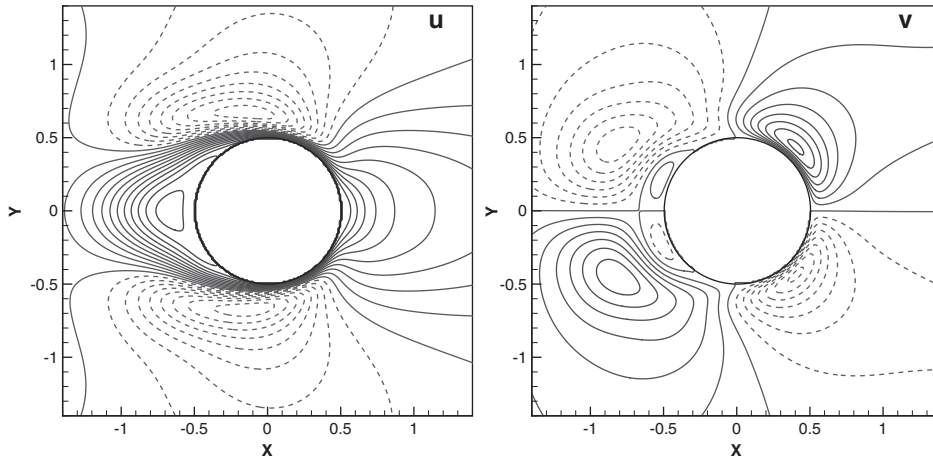


Figure 6. u - and v -contours around a circular cylinder under forced in-line oscillation in a fluid at rest. $Re = 100$ and $KC = 5$; phase angle $\theta = 90^\circ$; $-1.0 \leq u \leq 1.2$ with intervals of 0.1 and $-0.8 \leq v \leq 0.8$ with intervals of 0.1.

Boundary conditions for a clamped end at $y = 0$ and a free end at $y = L$ are given as follows:

$$w(0, t) = 0 \quad \text{and} \quad \left. \frac{\partial w}{\partial y} \right|_{y=0} = 0 \quad (13)$$

$$\left. \frac{\partial^2 w}{\partial y^2} \right|_{y=L} = 0 \quad \text{and} \quad \left. \frac{\partial^3 w}{\partial y^3} \right|_{y=L} = 0 \quad (14)$$

For each time step, the distribution of the pressure differences across the plate is calculated then Equation (11) is solved to estimate the deformation of the plate at the next time step using the finite difference method

$$\frac{w_j^{n+1} - 2w_j^n + w_j^{n-1}}{\Delta t^2} + C_1 \frac{w_{j+2}^n - 4w_{j+1}^n + 6w_j^n - 4w_{j-1}^n + w_{j-2}^n}{\Delta y^4} = -C_2(\Delta p)_j^n \quad (15)$$

After the deformation of the plate is decided at the new time step, the normal velocity distribution on the plate is estimated based on the time variation of the deformation. Using the calculated deformation and normal velocity distributions, the flow field is updated to estimate the pressure difference distribution at the next time step.

Glück *et al.* reported the computational results for the similar case [26, 27]. In their computations, a constant load is applied for a few initial time steps to excite the plate. In this study, the plate is initially deflected into the first eigenmode of the plate [24] instead of applying the artificial loads for a few initial steps. The present initial condition guarantees a steady oscillation without any change in the amplitude, if there is no effect of the fluid i.e. $C_2 = 0$. The n th eigenfunction ϕ_n of

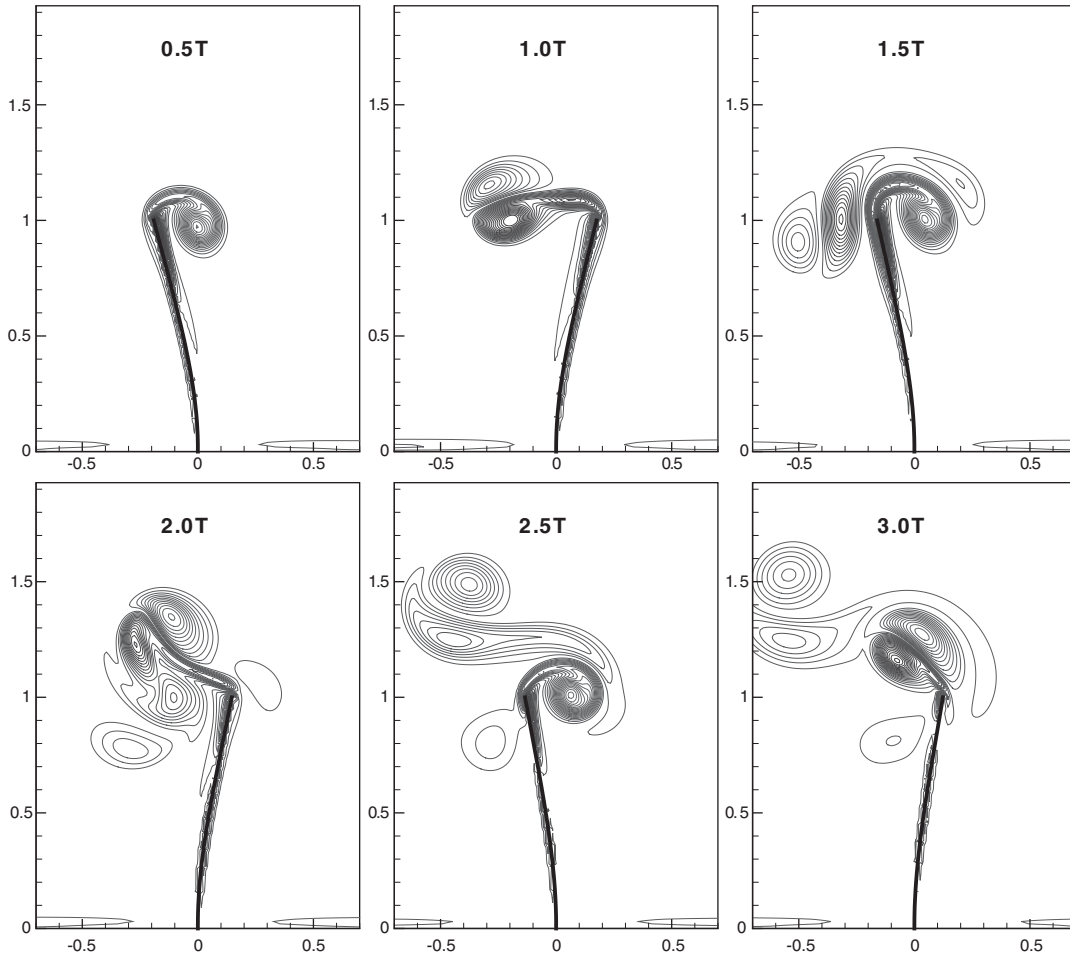


Figure 7. Time evolution of vorticity fields around a flexible plate oscillating freely in a fluid at rest. $Re=500$, $C_1=2.0$ and $C_2=0.05$; initial displacement at free end: 0.2; $-20 \leq \omega \leq 20$ with intervals of 1.0.

the plate is given as follows [28]:

$$\begin{aligned} \phi_n &= A_i \left[U(\lambda_n y) - \frac{S(\alpha_n)}{T(\alpha_n)} V(\lambda_n y) \right] \\ U(\lambda_n y) &= \frac{\cosh(\lambda_n y) - \cos(\lambda_n y)}{2}, \quad V(\lambda_n y) = \frac{\sinh(\lambda_n y) - \sin(\lambda_n y)}{2} \\ S(\alpha_n) &= \frac{\cosh \alpha_n + \cos \alpha_n}{2}, \quad T(\alpha_n) = \frac{\sinh \alpha_n + \sin \alpha_n}{2} \end{aligned} \quad (16)$$

where A_i is an amplitude constant, and $\lambda_n = \alpha_n/L$ and α_n are the solutions of $\cosh \alpha_n \cos \alpha_n + 1 = 0$.

The computational domain is $-60L \leq x \leq 60L$ and $0 \leq y \leq 60L$. The plate is clamped at the origin. The two non-dimensional parameters C_1 and C_2 are set to 2.0 and 0.05, respectively. For that

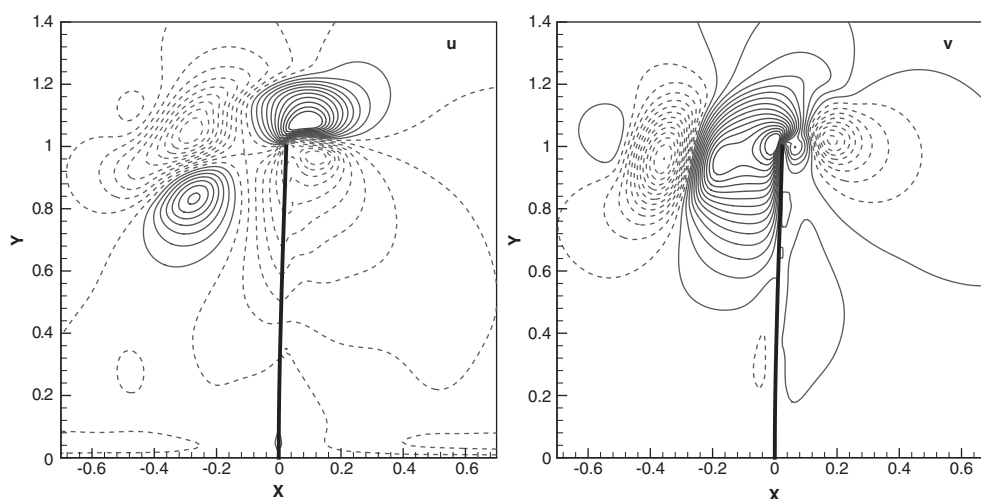


Figure 8. Instantaneous u - and v -contours around a flexible plate oscillating freely in a fluid at rest. $Re = 500$, $C_1 = 2.0$ and $C_2 = 0.05$; initial displacement at free end: 0.2; $t = 1.25$; $-1.0 \leq u \leq 1.0$ with intervals of 0.1 and $-1.5 \leq v \leq 1.5$ with intervals of 0.1.

value of the C_2 , the thickness of the plate is about $0.003L$ if a normal steel plate oscillates in the air. However, the actual material properties are not considered and the thickness of the plate is assumed to be zero in the computations regardless of the C_2 . The initial deformation A_i is $0.2L$. The Reynolds number based on the characteristic velocity U , which is used to define C_1 , is 500. For $-2L \leq x \leq 2L$ and $0 \leq y \leq 2L$, the grid spacing size is fixed then it is stretched by a factor of 1.05. To test grid independency of the computed results, the minimum grid spacing size is varied from 0.01 to 0.04 and the results are compared.

Figure 7 shows the time evolution of the vorticity fields around the oscillating plate. The instantaneous vorticity fields are included at the moments when the plate reaches the extreme displacements of the beginning three cycles. Due to the damping effects of neighbouring fluid, the amplitudes of the oscillation are decreasing gradually. The counter-rotating vortices are shed from the tip of the plate as the moving directions are alternated. Those vortices interact with each other and are shifted due to the flow induced by the movements of the plate. In Figure 8, instantaneous u - and v -contours are shown for the moment when the tip of the plate is passing $x = 0$ after one cycle. The u -velocity is continuous across the plate and is dominated by the movement of the plate to the left. However, the sharp discontinuity in the v -velocity across the plate can be clearly seen because of two boundary layers of the both sides.

A few computational results have been reported for the flow around a flexible plate [24, 26, 27]. Because of the diversity of the numerical schemes for the computations of the structure and fluid, each code has different limitations and it causes difficulties in comparisons with the previous results. However, the grid independencies of the present computations are investigated for both cases. To test grid independency of the present case, the time histories of location of the tip are compared for the three different size grids in Figure 9. Compared with the oscillation in a vacuum, which corresponds to the passive mode i.e. $C_2 = 0$, the results of the three grids predict virtually identical results for the damping of the oscillations and the changes in frequency of the

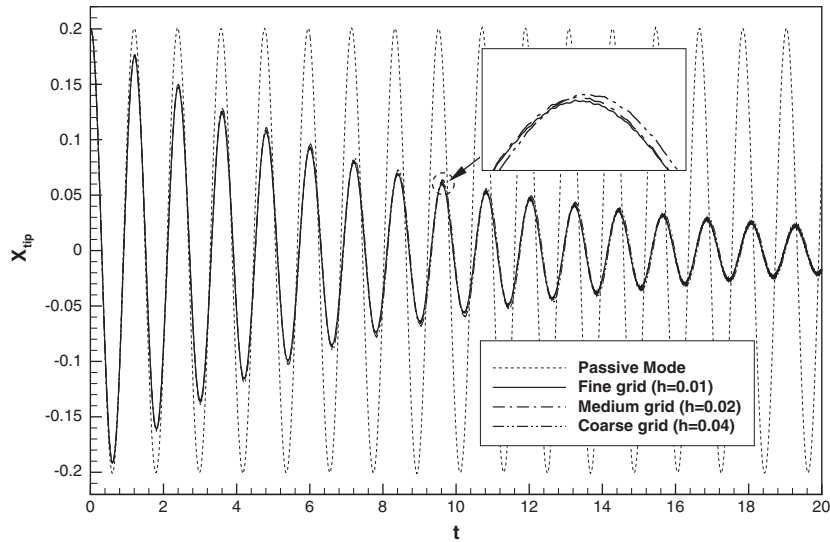


Figure 9. Grid independence tests for the computed displacement of free end of a flexible plate oscillating freely in a fluid at rest. Solid line: fine grid ($h = 0.01$); dash-dot: medium grid ($h = 0.02$) and dash-dot-dot: coarse grid ($h = 0.04$); $Re = 500$, $C_1 = 2.0$ and $C_2 = 0.05$; initial displacement at free end: 0.2.

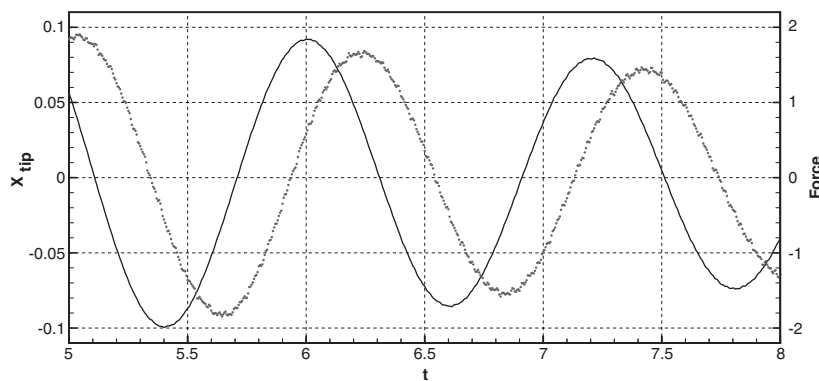


Figure 10. Phase shift between displacement of a flexible plate and fluid load. Solid line: displacement of a flexible plate; symbols: fluid load on the plate. $Re = 500$, $C_1 = 2.0$ and $C_2 = 0.05$; initial displacement at free end: 0.2.

oscillation. The damping of the oscillations implies that there is a phase shift between the motion of the plate and the fluid load. In Figure 10, the time history of the force acting on the plate (symbol) is compared with the displacement of the tip (line). It can be seen that the velocity of the plate dominates the time variation of the fluid load. Although the effects of the acceleration of the plate on the fluid load are smaller compared with the effects of the velocity, the acceleration causes the force of the opposite direction to the acceleration. The combined effects of the

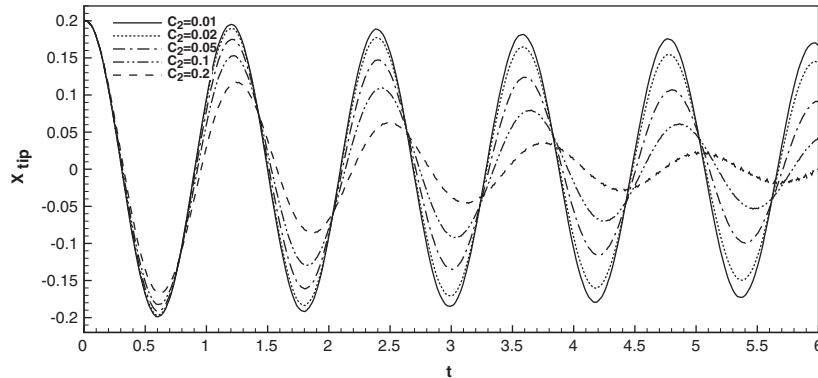


Figure 11. Effects of C_2 on oscillations of a flexible plate in a fluid at rest. $C_2 = 0.01, 0.02, 0.05, 0.1$ and 0.2 ; $Re = 500$, $C_1 = 2.0$; initial displacement at free end: 0.2 .

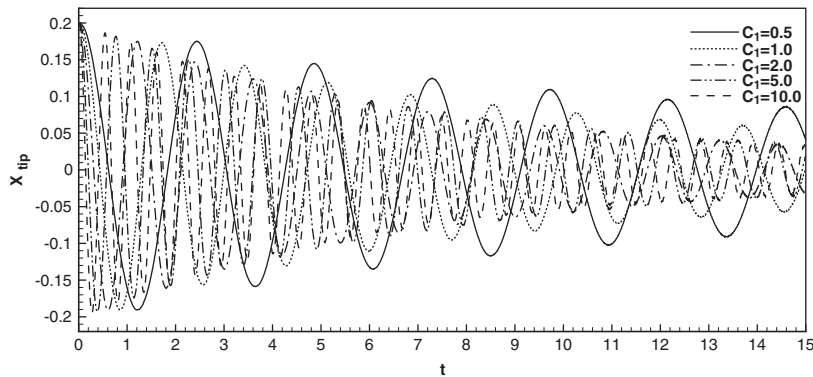


Figure 12. Effects of C_1 on oscillations of a flexible plate in a fluid at rest. $C_1 = 0.5, 1.0, 2.0, 5.0$ and 10.0 . $Re = 500$, $C_2 = 0.05$; initial displacement at free end: 0.2 .

velocity and the acceleration make the force zero slightly before the plate reaches its maximum deflection.

In Figure 11, the effects of the parameter C_2 on the oscillations of the plate are shown. The parameter C_2 represents the ratio of the inertia of the fluid to the inertia of the plate. As the fluid density increases, the oscillations are damped out rapidly and the period of the oscillations gets longer. The reasons of the variation in the period can be explained based on two different effects of the fluid load. Due to the damping effect of the fluid load, the period of the oscillation gets longer. Although the effects are smaller, the acceleration of the plate also influences the fluid load. The component of the fluid load that is proportional to the plate acceleration also increases the period of the oscillation due to the virtually increased inertia of the plate.

The parameter C_1 , which is a non-dimensionalized ratio of the bending stiffness to the inertia of the plate, is changed from 0.5 to 10 in Figure 12. The parameter C_1 controls primarily the period of the oscillations. However, the bigger C_1 results in the bigger damping of the oscillation because the velocity of the plate increases as the period decreases for the bigger C_1 .

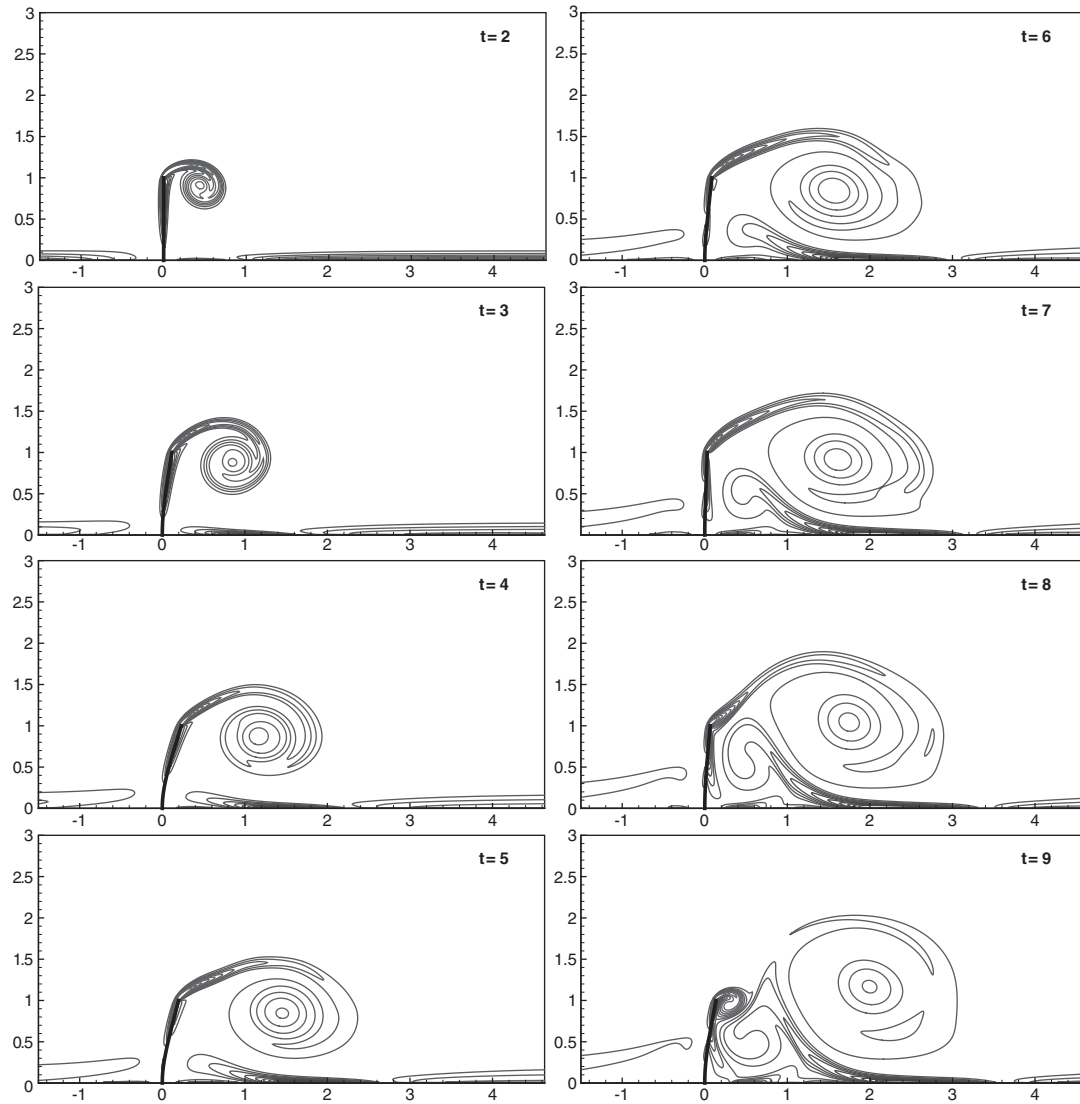


Figure 13. Time evolution of vorticity fields of flow over a flexible plate. $Re = 500$, $C_1 = 0.1$ and $C_2 = 0.1$; $-10 \leq \omega \leq 10$ with intervals of 1.

3.3. Cross flow over a flexible plate

The developed code is applied to simulate the cross flow over a flexible plate. Initially, the plate of length L is clamped at the origin and there is no deformation so that the free end is located at $x = 0$ and $y = L$. The computational domain is $-10L \leq x \leq 40L$ and $0 \leq y \leq 40L$. At $x = -10L$, the uniform inflow U is given and the no-slip boundary condition is applied at $y = 0$. For the outlet and upper boundary, the dependent variables are extrapolated from the fluid domain. The flow is accelerated linearly from the rest to the uniform inflow U until the non-dimensional time $t = 2$.

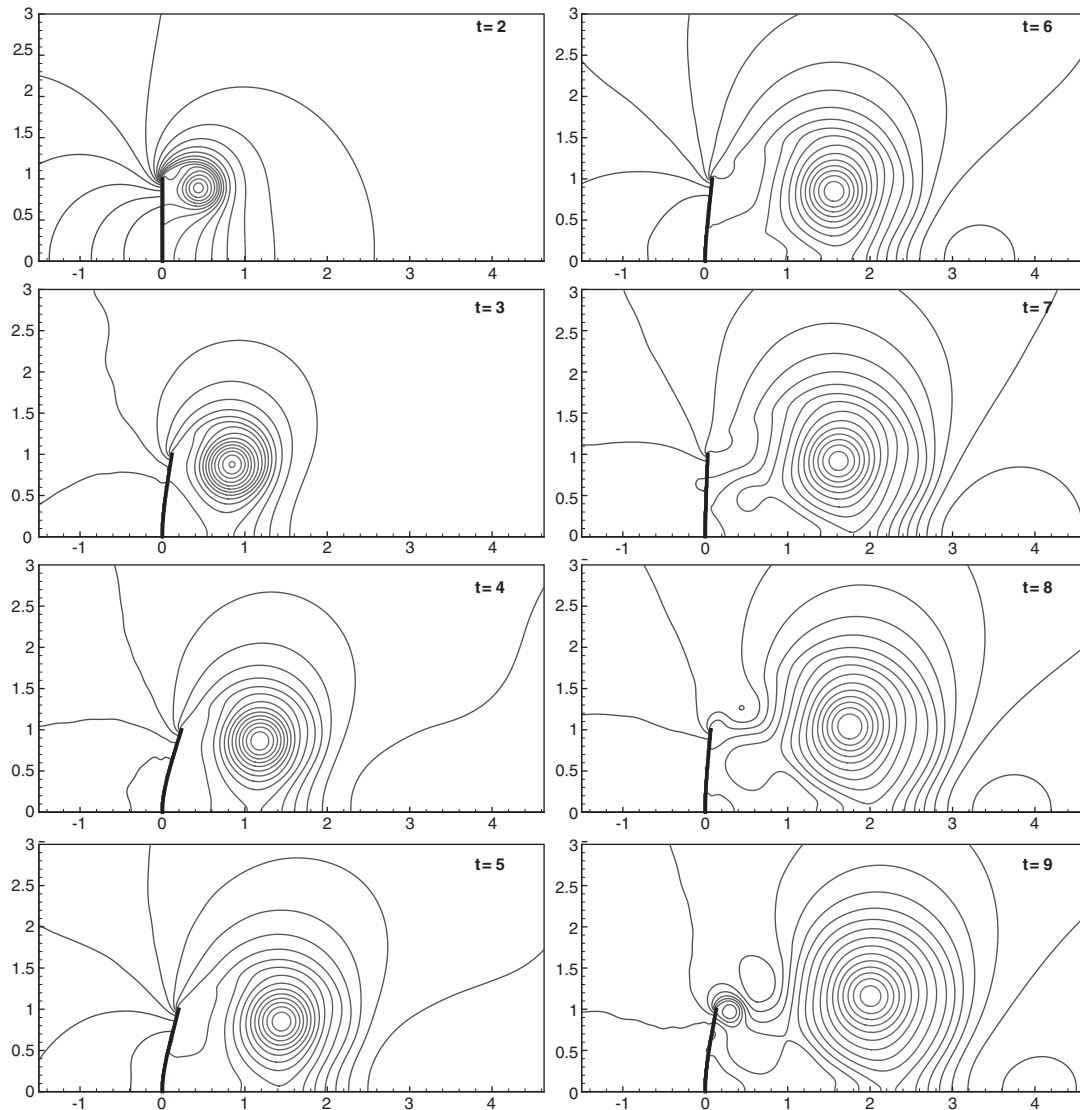


Figure 14. Time evolution of pressure fields of flow over a flexible plate. $Re = 500$, $C_1 = 0.1$ and $C_2 = 0.1$; $-2 \leq p \leq 2$ with intervals of 0.2.

During the acceleration of the inflow the plate is fixed, then the plate is released to deform by the fluid load at $t = 2$. The Reynolds number based on the plate length L and the uniform inflow U is 500. Both the parameters C_1 and C_2 are set to 0.1. For the region of $-2 \leq x \leq 4$ and $0 \leq y \leq 2$, the grid spacing is fixed then it is stretched by a factor of 1.02. To test grid independency of the computed results, three different size grids are used and the results are compared. For the fine, medium and coarse grid, the minimum grid sizes are 0.01, 0.02 and 0.04, respectively.

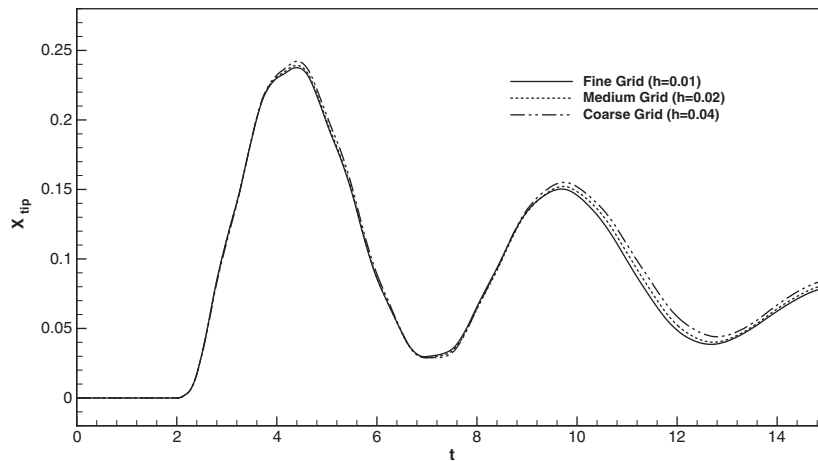


Figure 15. Grid independence tests for the computed displacement of free end of a flexible plate. Solid line: fine grid ($h = 0.01$); dashed line: medium grid ($h = 0.02$) and dash-dot-dot: coarse grid ($h = 0.04$); $Re = 500$, $C_1 = 0.1$ and $C_2 = 0.1$.

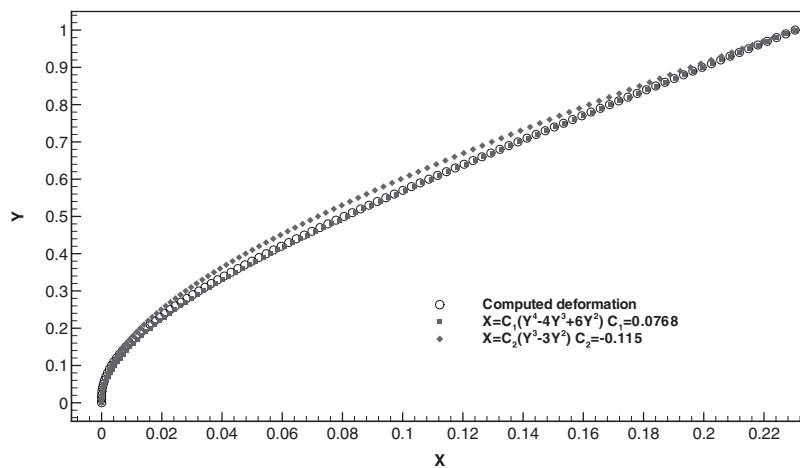


Figure 16. Comparisons of computed deformation (circle) with deformations under uniform (rectangles) and concentrated (diamond) loadings. $t = 4$; $Re = 500$, $C_1 = 0.1$ and $C_2 = 0.1$.

In Figures 13 and 14, the time evolutions of the vorticity and pressure fields are shown for $t = 2-9$. At $t = 2$, the vortex near the tip causes the shear flow on the backside of the plate. As the vortex grows and moves backwards, the vortex interacts with the bottom wall. Around $t = 4$, the plate reaches its extreme deformation. The extreme value of the tip deflection is about $0.23L$. The deflection at the tip for a cantilever with a uniform loading (ΔP) is $(\Delta P)L^4/8EI$. In this case, the non-dimensionalized stiffness $B/\rho_f U^2 L^3$ is $C_1/C_2 = 1$. It implies that the extreme deformation of $0.23L$ corresponds to a case of a cantilever under a uniform loading where the non-dimensional pressure difference Δp is about 1.84. Although the actual pressure difference Δp is a little smaller

than 1.84, the sudden release at $t = 2$ and the dynamic response of the plate cause the overshoot. After $t = 5$, the plate moves forward due to the restoring force of the plate. As the plate moves forward, fluids of the counter-clockwise vorticity, which are caused by the interaction of the main vortex with the bottom wall, occupy the space behind the plate. At $t = 9$, the second vortex is generated near the tip of the plate and the plate is pushed backward again by the fluid load.

In Figure 15, the computed time histories of the tip location are compared for the fine, medium and coarse grids. The agreements between the results of medium and fine grids are very good especially for $t \leq 10$. Since the fluid load of the initial stage causes strong transient response, the motion of the plate is different from the damped harmonic motion of the previous section. As the transient response of the plate decreases, the motion of the plate is dominated by its primary mode.

In Figure 16, the computed deformation of the plate at $t = 4$ is compared with the deformations of a cantilever under uniform and concentrated loadings where the deformations should be $C(y^4 - 4y^3 + 6y^2)$ and $C(y^3 - 3y^2)$, respectively. The constants C are set to 0.0768 and -0.115 , respectively, so that the deflections at the tip coincide. The computed deformation at $t = 4$ is more similar to the deformation of a cantilever under a uniform loading which causes the same tip deflection.

4. CONCLUSIONS

A code has been developed using the HCIB method and applied to simulate the interactions between a flexible plate and a surrounding fluid. A new criterion has been suggested to distribute the IB nodes based on the edges crossing the interface. It has been shown that the reconstruction of velocity at IB nodes distributed by the present criterion provides the adequate boundary conditions for the flow solver which is based on the hybrid staggered/non-staggered grid. In addition, the present criterion has been successfully applied to a zero-thickness body such as a thin plate.

To validate the developed code, the in-line oscillation of a circular cylinder in a fluid at rest has been simulated. The velocity profiles and vorticity and pressure fields have been compared with the experimental and other computational results. Good agreements are achieved.

The HCIB method has been successfully expanded to the fluid–structure interaction problems where the unsteady elastic deformation of the structure should be decided based on the fluid load. The oscillations of a flexible plate in the resting fluid and the flow over a flexible plate have been simulated. The grid convergence tests have been carried out for both cases using the three different size grids and the results of medium and fine grids show good agreements. Two non-dimensional parameters have been identified for the oscillations of a plate in a surrounding fluid, which are related to the ratios of the stiffness of the plate and the inertia of the fluid to the inertia of the plate. The effects of two non-dimensionalized parameters on the damping of the oscillations have been investigated.

ACKNOWLEDGEMENTS

This work was supported by the Underwater Vehicle Research Center (UVRC SM-42), Korea.

REFERENCES

1. Liu H, Kawachi K. A numerical study of undulating swimming. *Journal of Computational Physics* 1999; **155**:223–247.

2. Kuhl E, Hulshoff S, Borst R. An arbitrary Lagrangian–Eulerian finite-element approach for fluid–structure interaction phenomena. *International Journal for Numerical Methods in Engineering* 2003; **57**:117–142.
3. Cho JR, Lee SY. Dynamic analysis of baffled fuel-storage tanks using the ALE finite element method. *International Journal for Numerical Methods in Fluids* 2003; **41**:185–208.
4. Namkoong K, Choi HG, Yoo JY. Computation of dynamic fluid–structure interaction in two-dimensional laminar flows using combined formulation. *Journal of Fluids and Structures* 2005; **20**:51–59.
5. Luo H, Baum JD, Löhner R. On the computation of multi-material flows using ALE formulation. *Journal of Computational Physics* 2004; **194**:304–328.
6. Engel M, Griebel M. Flow simulation on moving boundary-fitted grids and application to fluid–structure interaction problems. *International Journal for Numerical Methods in Fluids* 2006; **50**:437–468.
7. Peskin CS. Flow patterns around heart valves: a numerical method. *Journal of Computational Physics* 1972; **10**:252–271.
8. Zhu L, Peskin CS. Simulation of a flapping flexible filament in a flowing soap film by the immersed boundary method. *Journal of Computational Physics* 2002; **179**:452–468.
9. Griffith BE, Peskin CS. On the order of accuracy of the immersed boundary method: higher order convergence rates for sufficiently smooth problems. *Journal of Computational Physics* 2005; **208**:75–105.
10. Pan D. An immersed boundary method for incompressible flows using volume of body function. *International Journal for Numerical Methods in Fluids* 2006; **50**:733–750.
11. Kim D, Choi H. Immersed boundary method for flow around an arbitrarily moving body. *Journal of Computational Physics* 2006; **212**:662–680.
12. Lee L, LeVeque RJ. An immersed interface method for incompressible Navier–Stokes equations. *SIAM Journal on Scientific Computing* 2003; **25**(3):832–856.
13. Li Z, Lubkin SR. Numerical analysis of interfacial two-dimensional Stokes flow with discontinuous viscosity and variable surface tension. *International Journal for Numerical Methods in Fluids* 2001; **37**:525–540.
14. Linnick ML, Fasel HF. A high-order immersed interface method for simulating unsteady incompressible flows on irregular domains. *Journal of Computational Physics* 2005; **204**:157–192.
15. Udaykumar HS, Shyy W, Rao MM. ELAFINT: a mixed Eulerian–Lagrangian method for fluid flows with complex and moving boundaries. *International Journal for Numerical Methods in Fluids* 1996; **22**:691–712.
16. Udaykumar HS, Mittal R, Khanna A. A sharp interface Cartesian grid method for simulating flows with complex moving boundaries. *Journal of Computational Physics* 2001; **174**:345–380.
17. Kirkpatrick MP, Armfield SW, Kent JH. A representation of curved boundaries for the solution of the Navier–Stokes equations on a staggered three-dimensional Cartesian grid. *Journal of Computational Physics* 2003; **184**:1–36.
18. Gilmanov A, Sotiropoulos F, Balaras E. A general reconstruction algorithm for simulating flows with complex 3D immersed boundaries on Cartesian grids. *Journal of Computational Physics* 2003; **191**:660–669.
19. Gilmanov A, Sotiropoulos F. A hybrid Cartesian/immersed boundary method for simulating flows with 3D, geometrically complex, moving bodies. *Journal of Computational Physics* 2005; **207**:457–492.
20. Yang J, Balaras E. An embedded-boundary formulation for large-eddy simulation of turbulent flows interacting with moving boundaries. *Journal of Computational Physics* 2006; **215**:12–40.
21. Shin S, Kim CK, Bai KJ. Numerical simulation on an interaction of a vortex street with an elliptical leading edge using an unstructured grid. *International Journal for Numerical Methods in Fluids* 2004; **44**:331–346.
22. Shin S. Internal wave computations using the ghost fluid method on unstructured grids. *International Journal for Numerical Methods in Fluids* 2005; **47**:233–251.
23. Dütsch D, Durst F, Becker S, Lienhart H. Low-Reynolds-number flow around an oscillating circular cylinder at low Keulegan–Carpenter numbers. *Journal of Fluid Mechanics* 1998; **360**:249–271.
24. Balint TS, Lucey AD. Instability of a cantilevered flexible plate in viscous channel flow. *Journal of Fluids and Structures* 2005; **20**:893–912.
25. Shames IH, Dym CL. *Energy and Finite Element Methods in Structural Mechanics*. Taylor & Francis: Bristol, PA, 1985.
26. Glück M, Breuer M, Durst F, Halfmann A, Rank E. Computation of fluid–structure interaction on lightweight structures. *Journal of Wind Engineering* 2001; **89**:1351–1368.
27. Glück M, Breuer M, Durst F, Halfmann A, Rank E. Computation of wind-induced vibrations of flexible shells and membranous structures. *Journal of Fluids and Structures* 2003; **17**:739–765.
28. Nowacki W. *Dynamics of Elastic Systems*. Chapman & Hall: London, 1963.